Elucidating Chiral Myosin-Induced Actin Dynamics: From Single Filament Behavior to Collective Structures

Takeshi Haraguchi[a], Kohei Yoshimura[a], Yasuhiro Inoue[b], Takuma Imi[a], Koyo Hasegawa[a], Taisei Nagai [a], Toshifumi Mori[c,d], Kenji Matsuno[e], and Kohji Ito[a,f,g,h,1]

[a] Department of Biology, Graduate School of Science, Chiba University, Chiba 263-8522, Japan

[b] Department of Micro Engineering, Kyoto University, Kyoto 615-8540, Japan

[c] Department of Applied Molecular Chemistry, Institute for Materials Chemistry and Engineering, Kyushu University, Fukuoka 816-8580 Japan

[d] Department of Interdisciplinary Engineering Sciences, Interdisciplinary Graduate School of Engineering Sciences, Kyushu University, Fukuoka 816-8580, Japan

[e] Department of Biological Sciences, Graduate School of Science, Osaka University, Osaka, 560-0043, Japan

[f] Membrane Protein Research Center (MPRC), Chiba University

[g] Molecular Chirality Research Center, Chiba University

[h] Plant Molecular Science Center, Chiba University

[1]To whom correspondence may be addressed. Email: k-ito@faculty.chiba-u.jp

Competing Interests Statement: The authors declare no competing interest.

Significance Statement

Myosins are essential motor proteins that drive intracellular transport, yet their ability to organize actin filaments into higher-order structures remains poorly understood. Here, we demonstrate that a plant myosin XI induces chiral curved motion of actin filaments and drives the spontaneous formation of stable, rotating actin rings through collective behavior. These structures, termed actin chiral rings (ACRs), emerge at actin concentrations approximating physiological conditions and show remarkable stability. Our findings uncover a previously unrecognized organizing principle of actin self-assembly driven by chiral myosin activity and provide a new framework for understanding how cytoskeletal chirality contributes to cellular organization across kingdoms.

Abstract

The myosin superfamily comprises over 70 classes, each with multiple subclasses, and shows substantial diversity in properties such as velocity, ATPase activity, duty ratio, and directionality. This functional diversity underpins the specialized roles of each myosin in various organisms, organs, and cell types. Recent studies have revealed that certain myosins induce chiral curved motions of actin filaments. However, this newly identified property remains largely unexplored. Here, we investigated this chiral motion *in vitro* using *Chara corallina* myosin XI (*Cc*XI), which drives fast counterclockwise (CCW) movement of actin filaments. This chiral motion arises from asymmetric displacement at the filament's leading tip, and its curvature depends on the surface density of myosin. Surprisingly, at near-physiological actin concentrations, actin filaments exhibiting chiral curved motion undergo collective motion, spontaneously forming a novel structure—termed the actin chiral ring (ACR)—that exhibits persistent CCW rotation. ACRs display remarkable stability, continuing to rotate at their formation site until ATP is depleted, while maintaining their structure even after rotation ceases. This stability is unprecedented among reported collective motions of cytoskeletal proteins driven by various motors. Our findings demonstrate that myosins with chiral activity can autonomously organize actin filaments into stable, chiral structures through collective dynamics, providing new insights into actin self-organization by unconventional myosins. This study advances our understanding of the diverse functional roles of unconventional myosins and introduces a new paradigm for cytoskeletal organization.

Abbreviations: ACR, actin chiral ring; *Cc*XI, *Chara corallina* myosin XI; MD, motor domain; SkII, skeletal muscle myosin II; CCW, counterclockwise; CW, clockwise; *Cb*XI-3, *Chara braunii* myosin XI-3; SI, supplementary information.

Introduction

Phylogenetic analyses of myosin motor domain (MD) sequences have revealed remarkable diversity within the myosin superfamily. To date, at least 79 distinct classes have been identified (1). These myosin classes and subclasses exhibit broad functional diversity in properties such as actin sliding velocity, actin-activated ATPase activity, duty ratio (the fraction of ATPase cycles during which the motor domain remains strongly bound to actin), and directionality of actin filament movement (2). Recently, a novel functional property of myosin has been reported: rat myosin IC and *Drosophila* myosin ID drive actin filaments in a counterclockwise (CCW) trajectory, resulting in chiral curved motions (3, 4). This chiral activity is particularly noteworthy because the motor domain of *Drosophila* myosin ID plays a critical role in establishing left-right asymmetry (chirality) of *Drosophila* cells and organs (4-7). However, the mechanistic link between the chiral activity of myosin ID and the emergence of cellular or organismal chirality remains poorly understood.

The motility properties of each myosin isoforms, such as sliding velocity and the directionality of actin filament movement, have been extensively analyzed using *in vitro* motility assays. In this method, myosin molecules are randomly immobilized onto a coverslip, and fluorescently labeled actin filaments are introduced along with ATP to visualize their movements (8). Although the filaments move in various directions across the surface, their velocity and directionality are consistent with those observed for the corresponding myosin isoforms *in vivo*. Therefore, *in vitro* motility assays serve as a reliable method for quantifying the velocities and directionality of myosin-driven actin movements. These assays typically use fluorescent actin at a concentration of 3×10^{-4}

mg/ml, which is approximately 1/1,000 of the intracellular actin concentration (9). Such low concentrations are employed to allow for the clear observation of individual actin filament trajectories.

Recently, a modified *in vitro* motility assay has been developed to allow tracking of individual actin filaments under conditions that approximate intracellular actin concentrations. This improvement was achieved by supplementing the assay buffer with non-fluorescent actin at physiological levels, together with a low concentration of fluorescently labeled actin. Remarkably, under these dense actin conditions, actin filaments driven by skeletal muscle myosin no longer exhibited random motions. Instead, they displayed collective behaviors characterized by coordinated movement. These collective dynamics manifested in diverse forms, including polar clusters, nematic streams, and swirling vortices. A common structural feature among these diverse forms was the parallel alignment of actin filaments along their longitudinal axes (10).

To date, *in vitro* studies of myosin-driven collective motion of actin filaments have primarily employed skeletal muscle myosin, also known as conventional myosin. However, *in vivo*, skeletal muscle myosin is confined to the sarcomeres of muscle cells and does not participate in collective cytoskeletal dynamics. In most other cell types—including plant cells and non-muscle animal cells—the movement of actin filaments is predominantly driven by unconventional myosins. These intracellular actin movements often display a relatively ordered orientation rather than random trajectories. It is therefore plausible that unconventional myosins contribute to this ordered intracellular actin alignment through collective motion. Given that the motile properties of

unconventional myosins differ from those of skeletal muscle myosin, the resulting collective motion patterns are also likely to be distinct.

The collective behavior of the active matter is strongly governed by the geometric shape and motility characteristics of its components. For rod-shaped active matter, such as those composed of elongated filaments, collective motion is predominantly driven by lateral interactions, resulting in alignment along the longitudinal axes. This phenomenon has been observed in the collective dynamics of actin filaments driven by skeletal muscle myosin, where filaments behave as linear rods and exhibit motion aligned with their long axes, as described previously (10-14). Recently, increasing attention has been directed toward the collective behavior of chiral active matter, in which the components either possess intrinsic chirality or exhibit chiral motion patterns(15, 16). FtsZ, a bacterial homolog of the eukaryotic protein tubulin, polymerizes into filaments. When these filaments are anchored to a lipid surface via FtsA, they exhibit a treadmill-like motion and adopt a chiral shape. As the concentration of FtsZ increases, these filaments self-organize into rotating chiral rings through collective motion. It has been proposed that the formation of these chiral rings results from lateral interactions between moving FtsZ filaments with chiral geometry (15, 17).

In this study, we demonstrate that *Cc*XI motor domain (MD) induces CCW actin movements. This chiral activity resembles that reported for rat myosin IC and *Drosophila* myosin ID (3, 4). However, unlike these class I myosins, *Cc*XI MD exhibits fast motility (18-20), enabling detailed analysis within a shorter time window. We show that myosins with chiral activity, such as *Cc*XI MD, possess a unique capacity to autonomously drive

133 the formation of highly stable, actin chiral structures—structures we term actin chiral
134 rings (ACRs)—through collective motion of actin filaments. This finding provides new
135 insights into the mechanisms of actin filament self-organization and expands our
136 understanding of the broader functional roles of unconventional myosins in cytoskeletal
137 dynamics.
138

Results

Chiral Curved Actin Motions by *Cc*XI

In the standard *in vitro* motility assay (Fig. 1A), *Cc*XI MD, a fast plant myosin XI(18-20), drove actin filaments in a counterclockwise (CCW) circular path when viewed from the actin side (clockwise (CW) when viewed from the objective lens side) (Fig. 1B: *Cc*XI MD and Movie S1). Similar CCW movements have been previously reported for actin filaments driven by mouse myosin IC (3) and *Drosophila* myosin ID (4). The curvature of actin movements driven by *Cc*XI MD was 17.0 ± 5.5 deg/µm (Fig. 1C: *Cc*XI MD), which exceeds the values reported for mouse myosin IC and *Drosophila* myosin ID using a similar assay (standard *in vitro* motility assay on glass surfaces) (3, 4). In contrast, actin filaments driven by rabbit skeletal muscle myosin II (SkII)—a widely used reference myosin—followed nearly straight trajectories, with an average curvature of 0.47 ± 8.8 deg/µm (Fig. 1B and C: Rab SkII).

To determine whether this chiral activity is a common feature among class XI myosins, we measured the curvature of the actin trajectories using *Cb*XI-3 (*Chara braunii* myosin XI-3) MD, which belongs to the same class as *Cc*XI (21). Although *Cb*XI-3 is a paralog of *Cc*XI and shares high sequence similarity (98%) and identity (88%) with *Cc*XI, the curvature of the actin trajectory induced by *Cb*XI-3 MD (3.1 ± 8.7 deg/µm) was significantly smaller than that induced by *Cc*XI MD. These results suggest that the curvature of the trajectory is determined by subtle variations in the myosin amino acid sequence, rather than by myosin class. This finding is consistent with previous reports indicating that only a subset of class I myosins generate curved actin trajectories whereas most do not (3, 4).

163

164 **Characterization of Chiral Curved Actin Motions**

165 To investigate how *Cc*XI-induced actin filament curvature depends on myosin density,
166 we performed a series of *in vitro* motility assays using chambers with a spacer thickness
167 of 0.24 mm. *Cc*XI MD was immobilized onto the coverslip surface, and increasing the
168 concentration of myosin introduced into the chamber resulted in a progressive increase in
169 actin filament curvature, which was observed up to a concentration of 0.5 μM (Fig. 1D).
170 At this concentration, the surface myosin density was estimated to be approximately 3.6
171 molecules per 10 × 10 nm^2 area. Given that the diameter of the myosin XI MD is
172 approximately 4 nm (21), this density likely corresponds to near-saturation of the
173 coverslip surface. Above this concentration, no further increase in curvature was detected,
174 suggesting that the effect plateaued due to saturation of available myosin-binding sites.
175 These results indicate that actin filament curvature increases in proportion to surface
176 myosin density until saturation is reached.

177

178 To elucidate the mechanism underlying this chiral curved motion, we tracked both the
179 leading and trailing ends of individual actin filaments. We found that both ends followed
180 the same trajectory (Fig. 1E), indicating that the curved motion is primarily generated by
181 asymmetric displacement at the filament's leading tip, while the remainder of the filament
182 passively follows the path without actively contributing to the curvature.

183

184 **Emergence of ACR through Collective Motion of Chiral Curved Actin**

185 Traditionally, standard *in vitro* motility assays have been conducted using actin
186 concentrations far below physiological levels, typically around 0.0005 mg/ml (9). These

low concentrations are preferred because higher concentrations of fluorescently labeled actin can obscure individual filaments, making it difficult to observe their movement. However, recent advances have enabled assays to be performed at actin concentrations closer to physiological levels (~1 mg/ml) by combining a low concentrations of fluorescently labeled actin with non-fluorescently labeled actin at physiological levels.

Using this approach, studies with skeletal muscle myosin have revealed that collective motion emerges even when myosin and actin filaments were randomly distributed on the coverslip. Remarkably, under these conditions, actin filaments exhibited highly organized collective motion, characterized by parallel filament arrays. Moreover, most filaments within these aligned arrays moved in the same direction, suggesting that collective motion not only facilitates parallel alignment of actin filaments but also promotes directional uniformity (10, 11, 14, 22-25).

Given that skeletal muscle myosin drives actin filaments along straight trajectories parallel to their longitudinal axes, whereas *Cc*XI induces chiral curved motion, we hypothesized that applying this modified motility assay with *Cc*XI under actin concentrations approximating physiological conditions might result in a different type of collective motion. To test this hypothesis, we performed the modified motility assay using *Cc*XI MD. We found that collective motion emerged effectively at initial actin concentrations between 0.1 and 0.3 mg/ml, with the strongest effects at 0.1 mg/ml. Therefore, subsequent experiments were conducted under this condition to maximize emergence of collective behavior.

211 The assay was initiated by adding a buffer containing 0.1 mg/ml actin (without ATP) to a
212 chamber precoated with *Cc*XI MD. After a 10-min incubation, an ATP-containing assay
213 buffer (without actin) was introduced to remove unbound filaments, and imaging was
214 initiated. Under these conditions, the actin filament density reached approximately 15 ±
215 4.1 filaments/μm² (*SI Appendix*, Fig. S1), consistent with values reported in previous
216 studies of skeletal muscle myosin II-driven collective actin motion (23).
217
218 Immediately after the ATP-containing buffer was added to the chamber, the *Cc*XI-driven
219 actin filaments moved randomly. However, after approximately 20 min, they self-
220 organized into a ring-like structure, in which the entire ring exhibited collective motion,
221 rotating predominantly in the CCW direction when viewed from the actin side. Notably,
222 this rotational direction matched the trajectories observed for individual actin filaments
223 at lower actin concentrations. We designated this structure the actin chiral ring (ACR)
224 (Fig. 2A, 2B and Movie S2). The formation of ACRs was confirmed even when Cy3-
225 labeled actin was used instead of rhodamine-phalloidin-labeled actin, ruling out the
226 possibility that ACR formation was an artifact of phalloidin labeling.
227
228 The dynamic process of ACR formation was continuously monitored, revealing distinct
229 intermediate stages. Although image clarity was partially compromised by
230 photobleaching due to the prolonged light exposure, key structural transitions were still
231 observable. Initially, actin filaments exhibited parallel stream-like flow that gradually
232 coalesced into nascent ring-like structures. These nascent rings subsequently developed
233 into fully formed ACRs, with their width increasing over time until reaching a stable state
234 (Movie S3 and Fig. 2C: *Cc*XI).

235

236 **Structural Characterization of ACRs**

237 We analyzed the structural characteristics of the ACRs. The ACRs exhibited limited size
238 variation, indicating a high degree of structural uniformity. The outer and inner diameters
239 were 21.8 ± 2.4 μm and 11.0 ± 2.3 μm, respectively (Fig. 3A). The inner curvature,
240 calculated from these inner diameters, was 10.0 ± 2.3 deg/μm (Fig. 3A: IC). Although
241 this value was slightly smaller than the curvature of individual actin filaments in the
242 absence of collective motion (17.0 ± 5.5 deg/μm, Fig. 1C), it closely matched it in
243 magnitude. This similarity, along with the consistent CCW direction of rotation, suggests
244 that *Cc*XI-induced curved actin motions are critical for ACR formation, although the
245 curvature appears to be slightly attenuated during collective motion.

246

247 In contrast, the outer curvature of the ACRs, calculated from the outer diameters, was 5.3
248 ± 0.6 deg/μm (Fig. 3A: OC), significantly lower than that of individual actin filaments.
249 This reduction in outer curvature likely imposes a physical size limit on the ACRs,
250 contributing to their nearly uniform dimensions. Furthermore, the consistent size of ACRs
251 below a certain threshold suggests that filament–filament affinity does not play a
252 significant role in their formation. If ACR formation were driven by filament affinity, the
253 structures would be expected to grow continuously over time without exhibiting a defined
254 size limit.

255

256 The ACRs exhibited remarkable temporal and spatial stability. Once formed, they
257 continued to rotate at the same location without positional displacement (Fig. 2B and
258 Movie S2). When external fluid flow was intentionally applied after formation, the ACRs

maintained their structure and continued to rotate at the same location, highlighting their structural integrity and robustness. Moreover, the ACRs preserved their ring-shaped architecture even after rotational motion ceased due to ATP depletion. Taken together, these observations underscore the exceptional stability of the ACR as a structural unit.

To analyze the movement of individual actin filaments within the ACR, we adjusted the ratio of Cy3-labeled to non-fluorescent actin (*SI Appendix*, Supplementary Materials and Methods) to enable clear visualization of each filament. Our observations revealed that a substantial majority (88%) of actin filaments within the ACR rotated in the CCW direction, while a minority (12%) exhibited CW rotation (Fig. 3B). This result is somewhat surprising, given that the entire ACR appears to rotate in the CCW direction (Movie S2), consistent with the observation that *Cc*XI drives individual filaments in a CCW direction (Fig. 1B and C). The CW-rotating filaments likely represent those that entered the ACR from the opposite direction and continued to move without reorienting, as discussed below. The observation that 88% of filaments within the ACR exhibit CCW motion reflects a strong bias toward unidirectional alignment. This proportion is notably higher than the 60–80% directional alignment during the collective motion of parallel actin filaments induced by skeletal muscle myosin (23). These results suggest that ACR formation facilitates more efficient unidirectional alignment of actin filaments compared to conventional collective motion systems.

To determine the number of actin filaments per ring width within the ACR, we employed the same approach of adjusting the ratio of Cy3-labeled to non-fluorescent actin (*SI Appendix*, Fig. S2). This method enabled us to estimate the number of filaments per ring

283 width, revealing an average of 320 ± 10 filaments and an estimated interfilament spacing
284 of approximately 22 ± 9.8 nm (Fig. 3C). This spacing—approximately three times the
285 diameter of a single actin filament—suggests that filaments within the ACR are relatively
286 spaced rather than densely packed. Notably, this interfilament distance is consistent with
287 the spacing (~20 nm) reported for collective actin motion driven by skeletal muscle
288 myosin in previous studies (25).
289
290 To investigate the dynamics of chiral curved actin filaments interacting with the ACR, we
291 again employed the method of adjusting the ratio of Cy3-labeled to non-fluorescent actin.
292 This approach enabled detailed observation of collision outcomes. When actin filaments
293 approached the ACR from the the direction opposite to its rotation, 80% were repelled,
294 10% were integrated into the ACR and began rotating in the CCW direction, and the
295 remaining 10% were incorporated but rotated in the CW direction (Fig. 3D, right). This
296 latter group likely represents the minority CW-rotating population observed within the
297 ACR, as noted above. In contrast, when actin filaments approached from the same
298 direction as the ACR's rotation, 90% were assimilated and adopted CCW rotation, while
299 the remaining 10% were excluded (Fig. 3D, left).
300
301 **Effects of Actin Bundling Protein and Methylcellulose on ACR Formation**
302 In the cellular environment, actin-binding proteins (ABPs) play an essential role in
303 modulating actin networks by bundling actin filaments. To investigate the influence of
304 ABPs on ACR formation, we focused on villin, a well-characterized actin-bundling
305 protein. In modified *in vitro* motility assays under high actin concentrations, the presence
306 of villin markedly accelerated ACR formation, reducing the time required from

307 approximately 20 min (in the absence of villin) to just a few minutes. The ACRs formed
308 in the presence of villin were significantly smaller, with an outer diameter of
309 approximately 5 μm—about quarter of the ~20 μm diameter observed without villin.
310 Notably, these smaller ACRs formed in the presence of villin maintained rotational
311 behavior at their formation site (Fig. 4A, Movie S4), similar to the ACRs formed in the
312 absence of villin. This observation suggests that villin-mediated size reduction does not
313 impair either the rotational stability or the self-organization process of ACRs.
314
315 Methylcellulose, a polymer widely used in *in vitro* studies to mimic intracellular
316 molecular crowding (26, 27), is known to promote actin bundling through the depletion
317 effect (28, 29). The presence of methylcellulose markedly altered ACR formation, leading
318 to the emergence of large, vortex-like ACRs with outer diameters reaching up to 100
319 μm—substantially larger than the ~20 μm diameter observed in its absence. These vortex-
320 like ACRs exhibited the same CCW rotation as those formed without methylcellulose
321 (when viewed from the actin side). However, they were unstable and rapidly disintegrated
322 after formation (Fig. 4B, Movie S5).
323
324 We next examined the combined effects of villin and methylcellulose on ACR formation.
325 In the presence of both factors, ACRs exhibited slightly larger diameters—approximately
326 30 μm—compared to the typical ~20 μm ACRs. The direction of rotation of these ACRs
327 was CCW, which was consistent with the direction observed under other conditions.
328 However, similar to the vortex-like ACRs formed in the presence of methylcellulose alone,
329 they were less stable and more prone to disintegration (Fig. 4C, Movie S6). These results
330 suggest that while villin accelerates ACR formation and reduces its size, methylcellulose

promotes the formation of larger and less stable ACR structures. Together, these two factors synergistically influence the size and stability of ACRs.

335 ## Discussion

336 In this study, we demonstrated that *Cc*XI drives actin filaments in the CCW direction and
337 that, at actin concentrations comparable to those found in cells, *Cc*XI induces the
338 autonomous formation of cell-sized ACRs through collective motion. Remarkably, ACRs
339 are exceptionally stable structures, maintaining continuous rotation at their formation site
340 until ATP depletion. Furthermore, even after ATP depletion, these structures preserved
341 their integrity, underscoring their robustness and stability as structural units.

342

343 **Insights into the Mechanism of CCW Actin Movement**

344 While most myosins move actin filaments along the filament axis, recent studies have
345 shown that certain class I myosins induce chiral curved motion, driving actin filaments in
346 a CCW direction (3, 4). However, the underlying mechanism of this motion remains
347 poorly understood, partly due to the extremely slow motility of class I myosins. To
348 investigate the mechanism of myosin-induced curved motion, we conducted a detailed
349 analysis of the CCW motion driven by *Cc*XI, a fast-moving myosin XI (18-20, 30, 31)(32),
350 which allowed for thorough analysis within a shorter time window. Our analysis revealed
351 that the trailing end of the filament followed the same path as the leading end (Fig. 1E),
352 indicating that the critical displacement for chiral curvature occurs predominantly at the
353 filament tip. The tip of the actin filament, characterized by its high degree of freedom, is
354 readily bent by oblique forces relative to the filament axis, likely generated by the power
355 stroke of *Cc*XI, as discussed below. In contrast, bending of other regions along the
356 filament is restricted by the strong, rigor-state binding of *Cc*XI, which anchors the
357 filament at both anterior and posterior contact points in these regions (*SI Appendix*, Fig.
358 S3).

Our study reveals a positive correlation between the curvature of actin filament trajectories and surface myosin density. This finding contrasts with the well-established inverse relationship between actin velocity and myosin density, in which increased myosin density typically reduces actin filament velocity. This velocity reduction is thought to result from strongly bound myosin molecules hindering the progression of filaments driven by other myosins performing power strokes (33, 34). In contrast, the observed increase in actin filament curvature with higher myosin density likely originates at the filament tips, where a higher myosin density induces more frequent bending events (Fig. 1E, *SI Appendix,* Fig. S4). As shown in Fig. S4, this tip-specific bending frequency scales with local myosin density, highlighting a mechanistic distinction from the velocity–density relationship.

Why does the leading tip of *Cc*XI-driven actin filaments move obliquely to the filament axis? To address this question, we must reconsider the mechanism by which myosin drives actin filaments. The lever-arm model, which is currently the most widely accepted explanation for myosin-driven actin movement, proposes that actin filament displacement is driven by a swinging motion of the lever arm. In this model, the lever arm undergoes a power stroke (swinging motion) relative to the actin filament axis, thereby propelling the filament forward (35). Myosins such as *Cc*XI, mouse myosin IC, and *Drosophila* myosin ID, which induce CCW actin motion, may achieve this by swinging their lever arms at an oblique angle relative to the actin filament axis. To test this hypothesis, we compared the rigor-state structures of acto-*Cc*XI MD, resolved by cryo-electron microscopy (32), with that of acto-SkII S1, also determined by cryo-electron microscopy (36). We initially

383 hypothesized that the lever-arm position of *Cc*XI in the rigor state would be oblique to
384 the actin filament. However, structural analysis revealed that the lever arm positions of
385 *Cc*XI and SkII in the rigor state were nearly identical, both aligning parallel to the actin
386 filament (*SI Appendix*, Fig. S5). Thus, the post-power stroke conformation alone cannot
387 account for the CCW actin movements driven by *Cc*XI.
388
389 In contrast, in the pre-power stroke state, *Cc*XI may adopt a lever-arm orientation that
390 deviates from the filament axis. This oblique configuration could result in a power stroke
391 that is inclined rather than parallel to the filament axis, thereby generating chiral curved
392 actin motion. A recent cryo-electron microscopy study of mouse myosin IC in both the
393 ADP-bound and the rigor states provides structural evidence supporting this hypothesis
394 (37). This study demonstrated that in the ADP-bound state, which corresponds to the pre-
395 power stroke state, mouse myosin IC exhibits a tilted lever arm relative to the filament
396 axis. In contrast, in the rigor state, which corresponds to the post-power stroke, the lever
397 arm is nearly parallel to the filament axis. These findings suggest that an oblique power
398 stroke, as observed in mouse myosin IC, is responsible for the generation of chiral curved
399 actin motion. Similarly, *Cc*XI may also adopt a pre-power stroke lever-arm orientation
400 that deviates from the filament axis, thereby producing an oblique power stroke and
401 subsequently inducing chiral curved motion.
402
403 **Mechanism of ACR Formation**
404 Under high actin concentration, actin filaments undergoing chiral curved motion driven
405 by *Cc*XI self-organized into ACRs through collective motion (Fig. 2A and B, Movies S2).
406 To understand how the ACRs are formed, it is instructive to apply insights from the well-

407 studied mechanism of SKII-driven collective motion to the context of *Cc*XI-driven
408 collective motion. Under similar high actin conditions, SKII induces the formation of
409 organized structures such as polar clusters, nematic streams, and swirling vortices (11, 12,
410 22-25). In these SKII-induced structures, the filaments are aligned parallel to one another.
411 This arrangement likely reflects the liquid crystalline properties of actin filaments: when
412 freely interacting at high densities, straight actin filaments behave as rod-like
413 macromolecules that naturally align along their longitudinal axes to minimize free energy
414 (Fig. 2C: SkII) (38, 39). Because of the differences in interaction effects between chiral
415 curved and straight actin filaments, it is not surprising that the collective motion of actin
416 filaments induced by *Cc*XI differs from that induced by SKII. Based on the liquid
417 crystalline properties of actin filaments, we propose that chiral curved actin filaments
418 driven by *Cc*XI initially align with the same polarity (Fig. 2C: *Cc*XI, middle), and
419 subsequently accumulate to form ACRs (Fig. 2C: *Cc*XI, right). Notably, the filament
420 behavior observed during ACR formation (Movie S3) closely resembles the schematic
421 model shown in Figure 2C (*Cc*XI).
422
423 Parallel streaming of actin filaments induced by SkII has been proposed to result from
424 orientation changes during filament collisions. However, previous studies have shown
425 that the angular adjustments during two-filament collisions are insufficient to account for
426 this phenomenon, indicating that interactions among multiple filaments are necessary to
427 establish parallel streaming (24, 25). Consistent with these findings, we also did not
428 observe significant angle changes in orientation during collisions between two chiral
429 curved actin filaments, similar to the case with straight filaments (24). These observations
430 suggest that effective alignment, whether in straight or chiral curved filaments, requires

multifilament interactions rather than simple binary collisions.

To examine the role of multifilament interactions, we simulated multifilament collisions using a simplified model, where the orientation of the leading edge of each filament adapted to that of neighboring filaments upon collision. Simulations with straight actin filaments resulted in bidirectional (nematic) streaming, rather than unidirectional (polar) streaming (Movie S7). In contrast, simulations with chiral curved actin filaments led to the emergence of curved polar arrays that self-organized into ACR-like structures (Movie S8), closely resembling the experimentally observed ACR formation process (Movie S3). The finding that polar orientation was more likely to emerge in simulations of chiral curved actin filaments is consistent with our experimental observations, where the collective motion of chiral curved actin filaments showed a significantly higher percentage of polar orientation (88%) compared with that of straight actin filaments (60-80%) (23) (Fig. 3B).

Collective motion of chiral curved actin filaments exhibits significantly greater structural uniformity and stability compared with that of straight actin filaments. In previous studies, straight actin filaments exhibited collective motions in various forms, such as waves and clusters, with variations in persistence and directionality (22-25). In contrast, chiral curved actin filaments consistently self-organized into ACRs, which invariably rotated in the CCW direction. This remarkable structural and directional consistency is likely a key factor contributing to the long-term stability of ACRs.

Similar self-organized chiral rings are also observed in the bacterial cytoskeletal system.

455 FtsZ, a bacterial tubulin homolog, polymerizes into curved filaments that exhibit chiral
456 treadmilling motion when anchored to lipid membranes via FtsA. At sufficiently high
457 concentrations, these curved filaments self-organize into chiral rotating rings *in vitro* (17,
458 40). Brownian dynamics simulations and coarse-grained modeling have further supported
459 the autonomous formation of these structures (15, 40). FtsZ plays a central role in
460 bacterial cytokinesis by assembling into the Z-ring at the future division site. These
461 findings suggest that the capacity of cytoskeletal proteins to form chiral rings through
462 collective motion may reflect a fundamental organizing principle of cytoskeletal systems.
463 Moreover, the formation of such chiral structures by cytoskeletal elements with intrinsic
464 chirality may represent a widespread and evolutionarily conserved mechanism across
465 diverse organisms.
466
467 **Functions of ACR in Cellular Dynamics**
468 ACR-like structures, referred to as acquosomes, have been identified in various plant cell
469 types, including *Arabidopsis*, tobacco BY2 cells, zinnia, and *Characean* algae. When
470 cytoplasmic extracts from *Characean* algae were observed under a dark-field microscope,
471 acquosomes exhibited rotational motion on the glass surface in the same direction as the
472 ACRs characterized in this study. Furthermore, negative-staining electron microscopy
473 revealed that these structures are composed of actin filament bundles with uniform
474 polarity (41). These findings suggest that the acquosomes formed *in vivo* possess
475 structural and dynamic properties analogous to those of ACRs reconstituted in this study
476 under *in vitro* conditions.
477
478 Acquosome formation has been reported to occur transiently during specific cellular

479 events such as the onset of growth or in response to injury, and this process depends on
480 myosin activity. In the case of pollen tube cells, for instance, acquosomes appear briefly
481 before the initiation of elongation and are subsequently reorganized into polarized actin
482 bundles that guide directional tip growth (42, 43)(44-46). Such polarized bundles are
483 essential for unidirectional cytoplasmic streaming, a fundamental mechanism for
484 intracellular transport in plant cells. Previous studies have demonstrated that these
485 structures can form autonomously through interactions between actin filaments and
486 myosin XI (47, 48), and that actin-bundling proteins such as plant villin facilitate their
487 formation by crosslinking filaments with uniform polarity (49). Our current findings
488 indicate that similarly polarized bundles can also form via ACRs, which emerge from the
489 collective motion of actin filaments driven by
490 myosin with chiral activity, *Cc*XI (Fig. 2B and Supplementary Movies 2 and 3). Moreover,
491 the presence of villin significantly accelerates this process (Fig. 4A, C and Supplementary
492 Movies 4 and 6). Integrating our findings with previous observations, we propose that
493 ACRs may serve as functional equivalents of acquosomes in organizing polarized actin
494 structures, with villin acting as a potential enhancer of this process *in vivo*.
495
496 *Drosophila* myosin ID, like *Cc*XI, drives the chiral curved motion of actin filaments (4).
497 It also plays a crucial role in establishing cellular and organ-level chirality (4-7), although
498 the underlying mechanism remains poorly understood. Given that ACRs are cytoskeletal
499 assemblies exhibiting chirality at the cellular scale, their formation by *Drosophila* myosin
500 ID could provide key insights into the mechanism by which myosin ID induces cell
501 chirality. Therefore, it is essential to determine whether *Drosophila* myosin ID can induce
502 ACR formation under physiological actin concentrations, as observed for *Cc*XI.

Although the functions of myosins have been extensively studied, little attention has been paid to their chiral activity, potentially leading to the oversight of myosins possessing this property. One reason for this oversight is that the chiral activity depends on myosin density and requires a sufficiently high concentration of myosin molecules, as demonstrated in Figure 1D. However, conventional *in vitro* motility assays are typically performed at low myosin densities to ensure smooth actin filament movement, thereby making the detection of chiral activity difficult. Consequently, despite numerous studies on *Cc*XI since 2003 (18-20, 30-32), its chiral activity has remained unidentified until the present study.

Uncovering the chiral activity of myosins opens new avenues for understanding how these motors regulate intracellular actin dynamics. Our findings demonstrate that myosin chiral activity can drive the autonomous formation of stable, highly ordered actin architectures, revealing an additional layer of complexity in cytoskeletal organization. This discovery broadens the functional landscape of myosins beyond conventional attributes such as velocity, ATPase activity, duty ratio, and directionality. Further exploration of myosin chiral activity in cellular contexts, including cytoskeletal organization and cell chirality, may provide key insights into its role in shaping cytoskeletal architecture and coordinating cellular organization.

524 **Materials and methods (see also *SI Appendix*, *Supplementary Materials*
525 *and Methods*)**
526
527 **Protein expression, and purification**
528 *Cc*XI MD and *Cb*XI-3 MD were expressed in insect cells (High Five^{TM}, Life
529 Technologies) and purified using nickel-affinity and FLAG-affinity resins as previously
530 described (20, 21). Further details are described in the *SI Appendix, Materials and*
531 *Methods.* Skeletal muscle myosin II was purified from rabbits as described previously
532 (50, 51). Skeletal muscle actin was purified from Chicken scapes using the method of
533 Spudich and Watt (52). Cy3-labeled skeletal muscle actin was prepared as described
534 previously (51, 53).
535
536 **Standard *in vitro* motility assay**
537 The standard *in vitro* motility assay was performed as previously described (20, 21).
538 Briefly, 0.2 mg/ml of anti-c-Myc antibody was perfused into the motility chamber. After
539 washing with assay buffer, 0.15 mg/ml of myosin molecules with a c-Myc epitope tag
540 were perfused into the chamber to immobilize the myosin molecules on the coverslip
541 surface using an anti-c-Myc antibody. Next, the assay chamber was infused with either
542 assay buffer containing 0.0003 mg/ml rhodamine-phalloidin-labeled actin or the same
543 concentration of phalloidin-labeled Cy3-actin. The composition of the assay buffer was
544 as follows: 25 mM Hepes-KOH (pH 7.4), 25 mM KCl, 4 mM MgCl2, 3 mM ATP, 10 mM
545 DTT, and an oxygen scavenging system (120 μg/ml glucose oxidase, 12.8 mM glucose,
546 and 20 μg/ml catalase). Observations of motility were conducted at 25°C.
547

548 **Modified *in vitro* motility assay at high actin concentration**

549 Myosin molecules were immobilized on the coverslip using an anti-c-Myc antibody as
550 described in the standard *in vitro* motility assay (19, 20)(21, 30, 54). The assay chamber
551 was subsequently infused with assay buffer without ATP, either containing 0.005–0.01
552 mg/ml rhodamine-phalloidin-labeled actin and 0.1 mg/ml actin or assay buffer containing
553 0.005 mg/ml phalloidin-labeled Cy3- labeled actin and 0.1 mg/ml actin. The actin used
554 was pre-treated with gelsolin (Sigma-Aldrich, product number: G8032) at a molar ratio
555 of 1000:1 to actin in the presence of 1 mM $CaCl_2$, resulting in an average length of
556 approximately 5 µm. It should be noted that the average length of actin filaments became
557 shorter due to severing events occurring during movement. After 10 min of incubation,
558 the assay buffer with ATP was infused to remove unbound filaments and observation
559 began. Cy3-labeled actin was prepared by labeling actin with Cy3-succinimide. To avoid
560 motility artifacts, the proportion of Cy3-labeled actin molecules within the filaments was
561 kept below 10%, as previously reported (51). The composition of the assay buffer was
562 the same as that used for the standard *in vitro* motility assay: 25 mM Hepes-KOH (pH
563 7.4), 25 mM KCl, 4 mM MgCl2, 3 mM ATP, 10 mM DTT, and an oxygen scavenging
564 system (120 µg/ml glucose oxidase, 12.8 mM glucose, and 20 µg/ml catalase) . In some
565 experiments, the concentration of KCl in the assay buffer was 150 mM. Observations of
566 motility were conducted at 25°C.

567

568 **Measuring the curvature of the trajectory of a single actin filament in the standard**
569 ***in vitro* motility assay**

570 An orientation difference-based method was used to calculate curvature from a set of
571 points. Specifically, the curvature was calculated by dividing the orientation angle

differences by the distance between two points using the orientation information of the point sequence (55). The X and Y coordinates of the leading end of a single actin filament were measured at 1 μm intervals over 21 points using Bohbo Soft (56). We then determined the curvature of the trajectory of a single actin filament from a set of 21 points spaced 1 μm apart by dividing the total angular variation by the total distance of movement across these 21 points. For each myosin type studied, curvature measurements were taken from approximately 30 actin filaments and then averaged to obtain the final values.

Acknowledgements

We would like to thank Dr. Junichiro Yajima and Dr. Takayuki Nishizaka for their helpful discussions. We also appreciate Dr. Shoji Baba and Dr. Kogiku Shiba for their support in using Bohbo Soft. We are grateful to Dr. Naruki Sato and Mr. Shinryu Wakatsuki for providing rabbit skeletal muscle myosin. This work was supported by a Grant-in-Aid for Scientific Research (JP 22K20623, JP 24K09482 to T.H., JP 23K23303, JP 23KK0254, JP 24K21756 to T.M., JP 15H05863, JP 24H01284 to K.M., JP 23K05710, JP 22H04833, JP 20K06583, JP 17K07436 to K.I., JP 1715H01309 to K.I.) from the Japan Society for the Promotion of Science (JSPS), by ALCA (KI) from the Japan Science and Technology Agency (JST). The calculations were partially carried out at the Research Center for Computational Sciences in Okazaki (24-IMS-C105) and using MCRP-M at the Center for Computational Sciences, University of Tsukuba.

Referecnces

1. M. Kollmar, S. Muhlhausen, Myosin repertoire expansion coincides with eukaryotic

diversification in the Mesoproterozoic era. *BMC Evol Biol* **17**, 211 (2017).

2. M. A. Hartman, J. A. Spudich, The myosin superfamily at a glance. *J Cell Sci* **125**, 1627-1632 (2012).
3. S. Pyrpassopoulos, E. A. Feeser, J. N. Mazerik, M. J. Tyska, E. M. Ostap, Membrane-bound myo1c powers asymmetric motility of actin filaments. *Curr Biol* **22**, 1688-1692 (2012).
4. G. Lebreton *et al.*, Molecular to organismal chirality is induced by the conserved myosin 1D. *Science* **362**, 949-952 (2018).
5. S. Hozumi *et al.*, An unconventional myosin in Drosophila reverses the default handedness in visceral organs. *Nature* **440**, 798-802 (2006).
6. P. Spéder, G. Ádám, S. Noselli, Type ID unconventional myosin controls left–right asymmetry in Drosophila. *Nature* **440**, 803-807 (2006).
7. K. Taniguchi *et al.*, Chirality in planar cell shape contributes to left-right asymmetric epithelial morphogenesis. *Science* **333**, 339-341 (2011).
8. S. J. Kron, J. A. Spudich, Fluorescent actin filaments move on myosin fixed to a glass surface. *Proc. Natl. Acad. Sci. USA.* **83**, 6272-6276 (1986).
9. S. J. Kron, Y. Y. Toyoshima, T. Q. P. Uyeda, J. A. Spudich, Assays for actin sliding movement over myosin-coated surfaces. *Methods Enzymol.* **196**, 399-416 (1991).
10. C.-P. Hsu, A. Sciortino, Y. A. de la Trobe, A. R. Bausch, Activity-induced polar patterns of filaments gliding on a sphere. *Nature Communications* **13**, 2579 (2022).
11. L. Huber, R. Suzuki, T. Kruger, E. Frey, A. R. Bausch, Emergence of coexisting ordered states in active matter systems. *Science* **361**, 255-258 (2018).
12. K. Ozawa *et al.*, Millimeter-sized belt-like pattern formation of actin filaments in solution by interacting with surface myosin in vitro. *Biophys Physicobiol* **16**, 1-8 (2019).
13. T. Iwase, Y. Sasaki, K. Hatori, Alignment of actin filament streams driven by myosin motors in crowded environments. *Biochimica et Biophysica Acta (BBA) - General Subjects* **1861**, 2717-2725 (2017).
14. A. Sciortino, A. R. Bausch, Pattern formation and polarity sorting of driven actin filaments on lipid membranes. *Proc Natl Acad Sci U S A* **118** (2021).
15. J. M. Moore, M. A. Glaser, M. D. Betterton, Chiral self-sorting of active semiflexible filaments with intrinsic curvature. *Soft Matter* **17**, 4559-4565 (2021).
16. B. Liebchen, D. Levis, Chiral active matter. *Europhysics Letters* **139**, 67001 (2022).
17. M. Loose, T. J. Mitchison, The bacterial cell division proteins FtsA and FtsZ self-organize into dynamic cytoskeletal patterns. *Nature Cell Biology* **16**, 38-46 (2014).
18. K. Ito *et al.*, Recombinant motor domain constructs of Chara corallina myosin display fast motility and high ATPase activity. *Biochemical and Biophysical Research Communications* **312**, 958-964 (2003).

19. K. Ito *et al.*, Kinetic mechanism of the fastest motor protein, Chara myosin. *J Biol Chem* **282**, 19534-19545 (2007).
20. K. Ito, Y. Yamaguchi, K. Yanase, Y. Ichikawa, K. Yamamoto, Unique charge distribution in surface loops confers high velocity on the fast motor protein Chara myosin. *Proceedings of the National Academy of Sciences* **106**, 21585-21590 (2009).
21. T. Haraguchi *et al.*, Discovery of ultrafast myosin, its amino acid sequence, and structural features. *Proceedings of the National Academy of Sciences* **119**, e2120962119 (2022).
22. T. Butt *et al.*, Myosin motors drive long range alignment of actin filaments. *J Biol Chem* **285**, 4964-4974 (2010).
23. V. Schaller, C. Weber, C. Semmrich, E. Frey, A. R. Bausch, Polar patterns of driven filaments. *Nature* **467**, 73-77 (2010).
24. R. Suzuki, C. A. Weber, E. Frey, A. R. Bausch, Polar Pattern Formation in Driven Filament Systems Require Non-Binary Particle Collisions. *Nat Phys* **11**, 839-843 (2015).
25. R. Suzuki, A. R. Bausch, The emergence and transient behaviour of collective motion in active filament systems. *Nat Commun* **8**, 41 (2017).
26. F. Huber, D. Strehle, J. Schnauß, J. Käs, Formation of regularly spaced networks as a general feature of actin bundle condensation by entropic forces. *New Journal of Physics* **17**, 043029 (2015).
27. J. Schnauß *et al.*, Transition from a Linear to a Harmonic Potential in Collective Dynamics of a Multifilament Actin Bundle. *Physical Review Letters* **116**, 108102 (2016).
28. S. Köhler, O. Lieleg, A. R. Bausch, Rheological Characterization of the Bundling Transition in F-Actin Solutions Induced by Methylcellulose. *PLOS ONE* **3**, e2736 (2008).
29. M. Miyazaki, M. Chiba, H. Eguchi, T. Ohki, S. i. Ishiwata, Cell-sized spherical confinement induces the spontaneous formation of contractile actomyosin rings in vitro. *Nature Cell Biology* **17**, 480-489 (2015).
30. M. Tominaga *et al.*, Cytoplasmic streaming velocity as a plant size determinant. *Dev Cell* **27**, 345-352 (2013).
31. T. D. Schindler, L. Chen, P. Lebel, M. Nakamura, Z. Bryant, Engineering myosins for long-range transport on actin filaments. *Nat Nanotechnol* **9**, 33-38 (2014).
32. P. V. Ruijgrok *et al.*, Optical control of fast and processive engineered myosins in vitro and in living cells. *Nature Chemical Biology* **17**, 540-548 (2021).
33. Y. Y. Toyoshima, S. J. Kron, J. A. Spudich, The myosin step size: measurement of the unit displacement per ATP hydrolyzed in an *in vitro* assay. *Proc. Natl. Acad. Sci. USA* **87**, 7130-7134 (1990).
34. K. Ito, X. Liu, E. Katayama, T. Q. Uyeda, Cooperativity between two heads of dictyostelium myosin II in in vitro motility and ATP hydrolysis. *Biophys. J.* **76**, 985-992

(1999).

35. J. Robert-Paganin, O. Pylypenko, C. Kikuti, H. L. Sweeney, A. Houdusse, Force Generation by Myosin Motors: A Structural Perspective. *Chem Rev* **120**, 5-35 (2020).

36. T. Fujii, K. Namba, Structure of actomyosin rigour complex at 5.2 A resolution and insights into the ATPase cycle mechanism. *Nat Commun* **8**, 13969 (2017).

37. S. S. Chavali, P. J. Carman, H. Shuman, E. M. Ostap, C. V. Sindelar, High-resolution structures of Myosin-IC reveal a unique actin-binding orientation, ADP release pathway, and power stroke trajectory. *Proceedings of the National Academy of Sciences* **122**, e2415457122 (2025).

38. B. Gentry, D. Smith, J. Käs, Buckling-induced zebra stripe patterns in nematic F-actin. *Phys Rev E Stat Nonlin Soft Matter Phys* **79**, 031916 (2009).

39. R. Zhang, N. Kumar, J. L. Ross, M. L. Gardel, J. J. de Pablo, Interplay of structure, elasticity, and dynamics in actin-based nematic materials. *Proc Natl Acad Sci U S A* **115**, E124-e133 (2018).

40. Z. Dunajova *et al.*, Chiral and nematic phases of flexible active filaments. *Nature Physics* **19**, 1916-1926 (2023).

41. S. Higashi-Fujime, Active movement in vitro of bundle of microfilaments isolated from Nitella cell. *Journal of Cell Biology* **87**, 569-578 (1980).

42. S. C. Tiwari, V. S. Polito, Spatial and temporal organization of actin during hydration, activation, and germination of pollen inPyrus communis L.: a population study. *Protoplasma* **147**, 5-15 (1988).

43. A. O. Frost, A. W. Roberts, Cortical actin filaments fragment and aggregate to form chloroplast-associated and free F-actin rings in mechanically isolatedZinnia mesophyll cells. *Protoplasma* **194**, 195-207 (1996).

44. A. P. Smertenko, M. J. Deeks, P. J. Hussey, Strategies of actin reorganisation in plant cells. *Journal of Cell Science* **123**, 3019-3028 (2010).

45. F. Vogler, S. Sprunck, F-actin forms mobile and unwinding ring-shaped structures in germinating Arabidopsis pollen expressing Lifeact. *Plant Signaling & Behavior* **10**, e1075684 (2015).

46. I. Foissner, G. O. Wasteneys, The characean internodal cell as a model system for studying wound healing. *J Microsc* **247**, 10-22 (2012).

47. H. Ueda *et al.*, Myosin-dependent endoplasmic reticulum motility and F-actin organization in plant cells. *Proceedings of the National Academy of Sciences* **107**, 6894-6899 (2010).

48. R. E. Goldstein, J. W. van de Meent, A physical perspective on cytoplasmic streaming. *Interface Focus* **5**, 20150030 (2015).

49. T. Shimmen, E. Yokota, Cytoplasmic streaming in plants. *Curr Opin Cell Biol* **16**, 68-72 (2004).
50. K. Yamamoto, Identification of the site important for the actin-activated MgATPase activity of myosin subfragment-1. *J. Mol. Biol.* **217**, 229-233 (1991).
51. S. Rula *et al.*, Measurement of enzymatic and motile activities of Arabidopsis myosins by using Arabidopsis actins. *Biochemical and Biophysical Research Communications* **495**, 2145-2151 (2018).
52. J. A. Spudich, S. Watt, The regulation of rabbit skeletal muscle contraction. I. Biochemical studies of the interaction of the tropomyosin-troponin complex with actin and the proteolytic fragments of myosin. *J. Biol. Chem.* **246**, 4866-4871 (1971).
53. S. T. Kijima, K. Hirose, S. G. Kong, M. Wada, T. Q. Uyeda, Distinct Biochemical Properties of Arabidopsis thaliana Actin Isoforms. *Plant Cell Physiol* **57**, 46-56 (2016).
54. T. Haraguchi *et al.*, Functional Diversity of Class XI Myosins in Arabidopsis thaliana. *Plant Cell Physiol* **59**, 2268-2277 (2018).
55. M. van Ginkel, J. Weijer, L. Van Vliet, P. Verbeek, *Curvature Estimation from Orientation Fields* (1999).
56. K. Shiba, Y. Mogami, S. Baba, Ciliary Movement of Sea-urchin Embryos. *Nat Sci Rep Ochanomizu Univ* **53** (2001).

Figure legends

Figure 1. Chiral curved motion of actin filaments driven by *Cc*XI in the standard *in vitro* motility assay. (*A*) Schematic diagram showing the standard *in vitro* motility assay. Myosin molecules were randomly immobilized on a coverslip, and fluorescently labeled actin filaments are added along with ATP to visualize filament motion. (*B*) Representative trajectories of actin filaments over a 5-second interval driven by *Chara corallina* myosin XI MD (*Cc*XI MD) and rabbit skeletal muscle myosin II (Rab SKII). The color gradient from red to purple indicates the progression of time from 0 to 5 seconds. (*C*) Histogram showing the distribution of actin filament curvatures in a standard *in vitro* motility assay with *Cc*XI MD and Rab SKII. Curvature (degrees per micrometer) was calculated from orientation changes at 1 μm intervals over 21 points along individual filaments. Positive

curvature values indicate CCW movement when viewed from the actin side. Each distribution represents measurements from 30 actin filaments per myosin condition. (see *SI Appendix*, Supplementary Materials and Methods). (*D*) Dependence of filament curvature on surface myosin concentration in a standard *in vitro* motility assay with *Cc*XI MD. The x-axis represents the myosin concentration (μM) applied to a chamber with a spacer thickness of 0.24 mm. The y-axis shows the mean filament curvature ± standard deviation (n = 27–30 filaments per condition). (*E*) Overlay of the trajectories of the leading (red) and the trailing (blue) ends of a single actin filament in a standard *in vitro* motility assay with *Cc*XI MD. The trailing end follows the same path as the leading end, indicating that curvature is generated primarily at the filament tip and is maintained along its length.

Figure 2. Autonomous formation of ACRs through the collective motion of chiral curved actin filaments driven by *Cc*XI in the modified *in vitro* motility assay. (*A*) Schematic illustration of ACR formation under conditions with elevated actin filament density. ACRs emerged within approximately 20 min after ATP addition, exhibiting CCW rotation when viewed from the actin side and CW rotation when viewed from the lens side. (*B*) Fluorescence microscopic images of fully formed ACRs. Once formed, the ACRs rotated continuously in the CCW direction at the same location where they initially developed.. The corresponding video is provided as Supplementary Movie 2. (*C*) Schematic representation of the formation process of collective actin motion under elevated actin filament density. ***Cc*XI**: Upon ATP addition, individual actin filaments driven by CcXI initially exhibited CCW chiral curved trajectories and progressively aligned into a parallel stream-like collective motion. These filaments then gradually assembled into ring-shaped structures, which subsequently rotated in the CCW direction. **SKII:** For comparison, a schematic of the collective motion of actin filaments driven by skeletal muscle myosin II (SkII), as reported in previous studies, is shown. In contrast to

763 *Cc*XI, SkII drives straight actin filaments that form parallel streams without ring
764 formation.
765
766 **Figure 3. Analysis of actin filament motion within ACR structures.** (*A*) Quantification
767 of the outer and inner diameters of the ACRs and the width of the ring. The outer and
768 inner diameters were measured by fitting circles using ImageJ. The data represent the
769 mean ± standard deviation of 120 ACRs. Except for actin concentration, all assay
770 conditions were identical to those used in the standard *in vitro* motility assay for
771 measuring single-filament curvature, including a solution containing 25 mM Hepes-KOH
772 (pH 7.4), 25 mM KCl, 4 mM $MgCl_2$, 3 mM ATP, and 10 mM DTT. (*B*) Directional
773 analysis of 90 actin filaments (AFs) from six ACR rings revealed that 79 AFs (88%)
774 moved in CCW direction, while 11 AFs (12%) moved in CW direction. This analysis was
775 conducted by reducing the ratio of Cy3-labeled actin, as described in the SI *Appendix*,
776 *Supplementary Materials and Methods*). (*C*) The filament density within ACRs was
777 estimated by lowering the proportion of Cy3-labeled actin, as illustrated in Fig. S2. Across
778 20 ACRs, the number of filaments per ring width averaged 320 ± 20, with an inter-
779 filament spacing of approximately 22 ± 9.8 nm. These values indicate relatively sparse
780 filament packing within the ring structure. (*D*) Outcomes of filament-ACR collisions
781 depending on the approach direction. (Left) When AFs approached in the same direction
782 as ACR rotation,, 90% were assimilated into the ACR and began rotating CCW, while
783 10% are ejected. (Right) When AFs approached from the opposite direction of ACR
784 rotation, 80% are repelled, 10% were incorporated and rotated CCW, and 10% were
785 incorporated but rotated CW. The latter population likely corresponds to the minority
786 CW-rotating filaments observed in (B). Each category was quantified based on
787 observations of 30 AFs for each direction.
788
789 **Figure 4. Effects of Actin Bundling Protein and Methylcellulose on ACR Formation**

(*A*) Formation of ACRs in the presence of villin. To assess the impact of actin-bundling proteins on ACR formation, 1.5 μM villin was added to the modified *in vitro* motility assay. Within 1 to 2 min after the start of the reaction, numerous small ACRs with outer diameters of approximately 5 μm appeared, which were rotating in CCW direction. These smaller ACRs exhibited robust and continuous CCW rotation at their formation sites, resembling the behavior of ACRs formed without villin. The video corresponding to Fig. 4(A) is available as Supplementary Movie 4, illustrating the dynamic process shown in this figure. (*B*) Formation of ACRs in the presence of methylcellulose. To mimic intracellular molecular crowding, 0.5% methylcellulose was included in the assay. This condition led to the emergence of large, vortex-like ACRs with outer diameters of approximately 100 μm appeared. These large, vortex-like ACRs rotated in CCW direction, similar to ACRs formed in the absence of methylcellulose. However, unlike ACRs formed without methylcellulose, these structures were unstable and disintegrated shortly after formation. The video corresponding to Fig. 4(B) is available as Supplementary Movie 5, illustrating the dynamic process shown in this figure. (*C*) Formation of ACRs in the combined presence of villin and methylcellulose. When both 1.5 μM villin and 0.5% methylcellulose were added, the resulting ACRs exhibited intermediate diameters of approximately 60 μm. Similar to other conditions, these ACRs rotated in CCW direction. However, as observed with methylcellulose alone, these large ACRs were unstable and rapidly disintegrated shortly after formation. The video corresponding to Fig. 4(C) is available as Supplementary Movie 6, illustrating the dynamic process shown in this figure.

Fig. 1

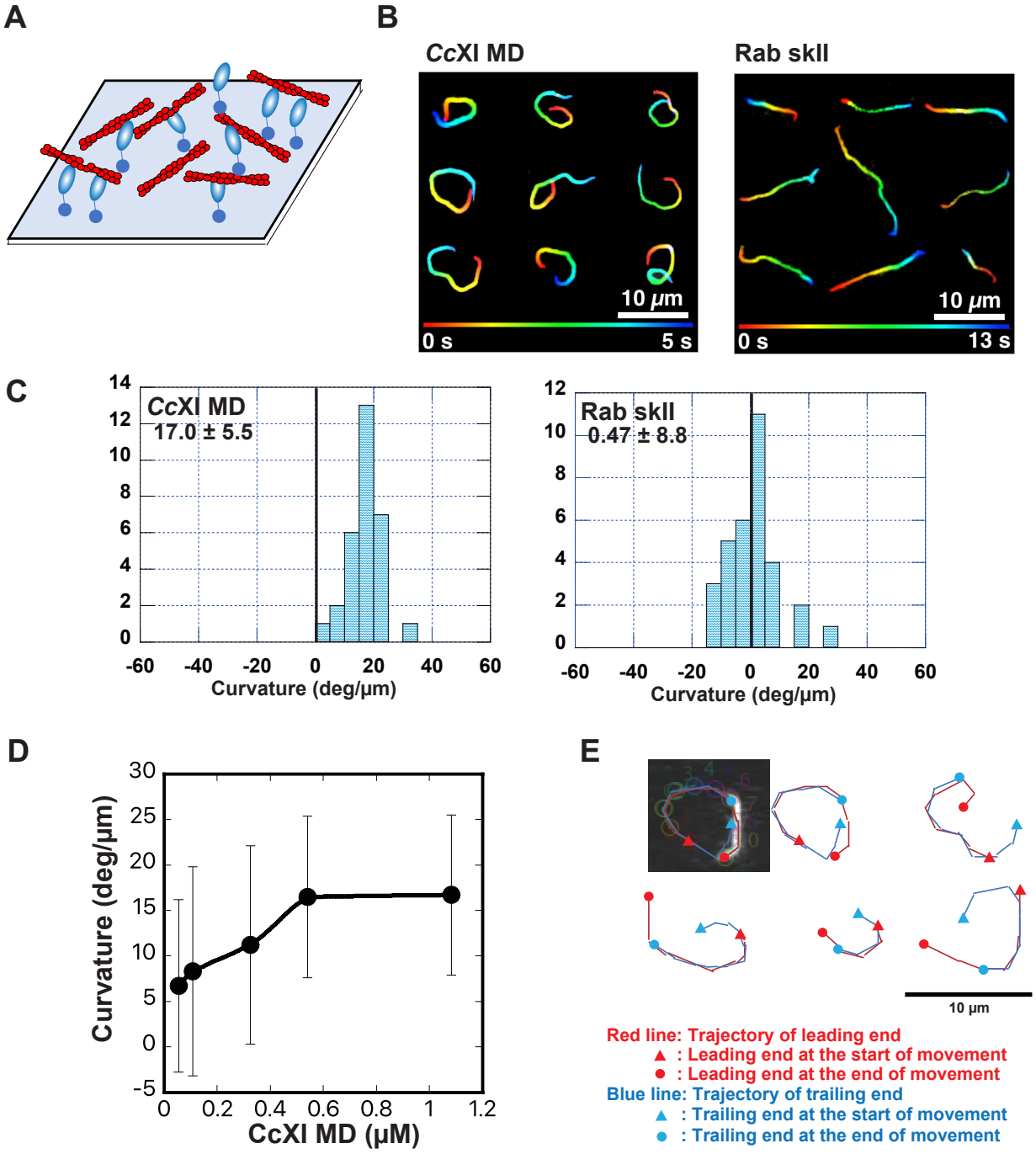
A
B
CcXI MD
Rab skII
10 μm
0 s
5 s
10 μm
0 s
13 s
C
CcXI MD
17.0 ± 5.5
Curvature (deg/μm)
Rab skII
0.47 ± 8.8
Curvature (deg/μm)
D
Curvature (deg/μm)
CcXI MD (μM)
E
10 μm
Red line: Trajectory of leading end
▲ : Leading end at the start of movement
● : Leading end at the end of movement
Blue line: Trajectory of trailing end
▲ : Trailing end at the start of movement
● : Trailing end at the end of movement

Fig. 2

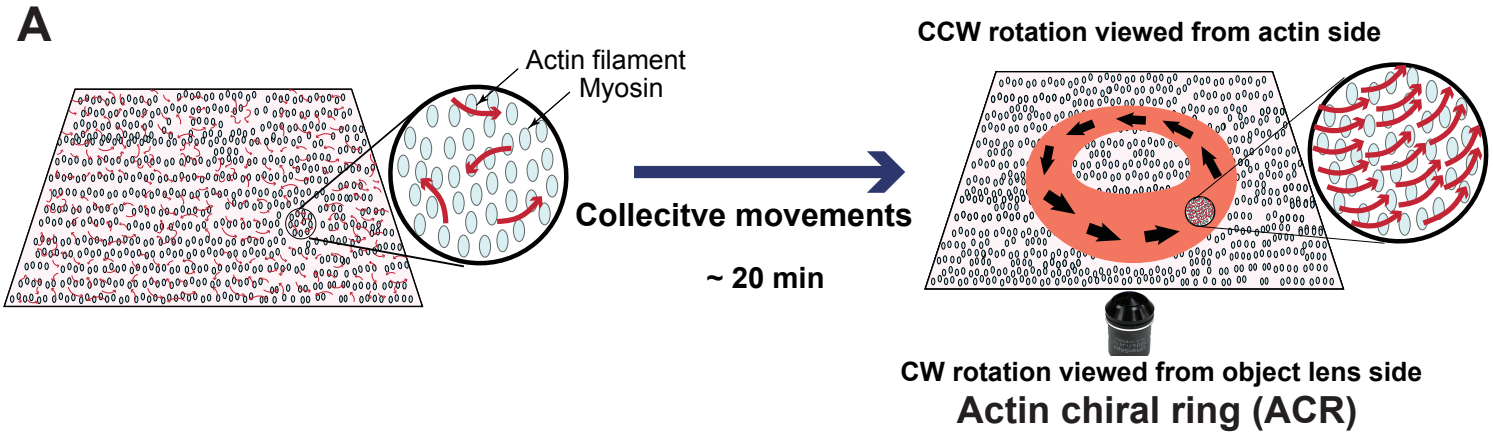

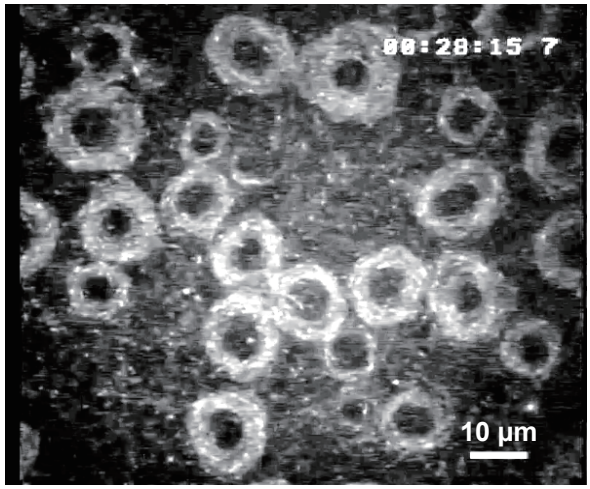

Fluorescence microscopic images of ACRs

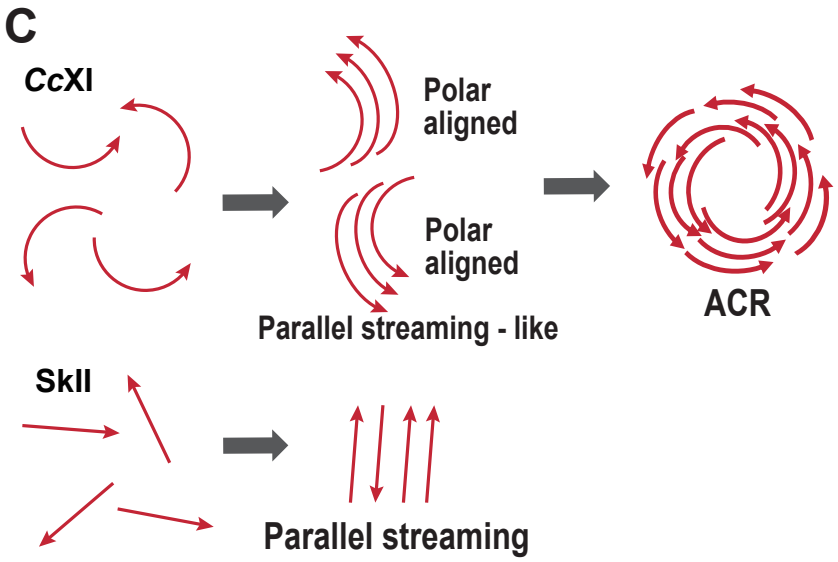

Fig. 3

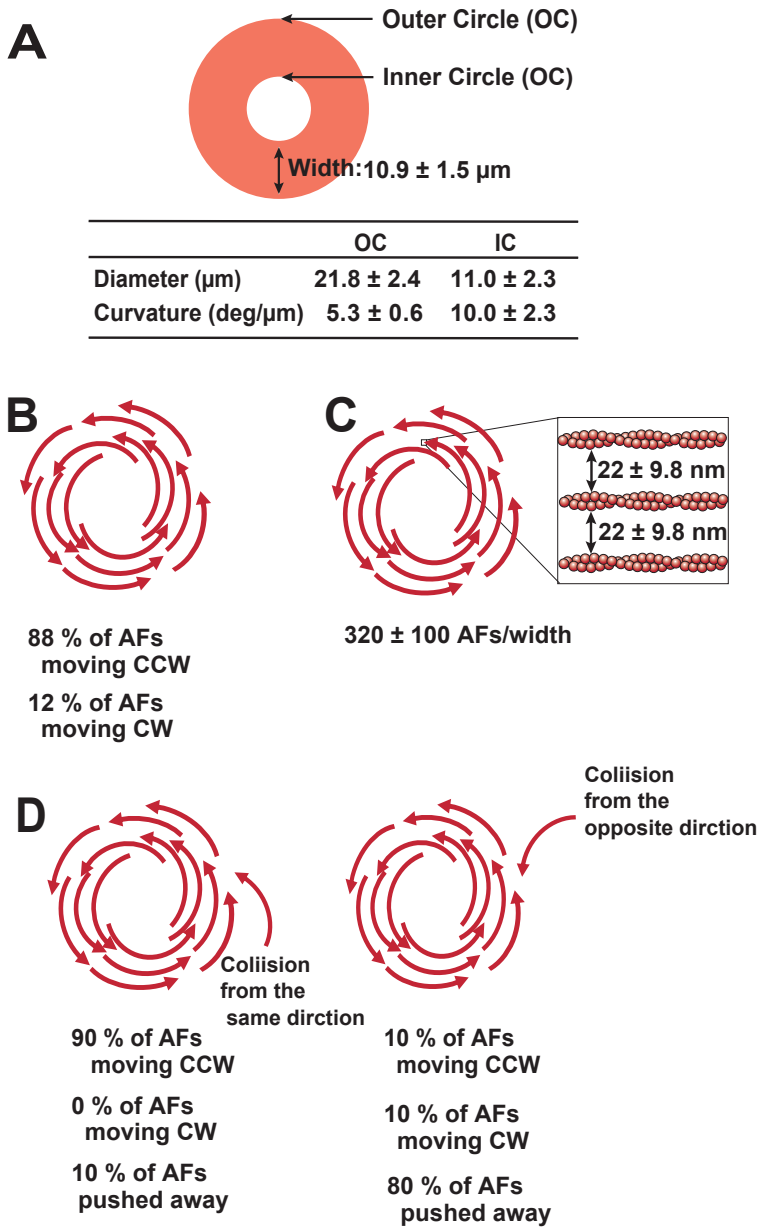

	OC	IC
Diameter (μm)	21.8 ± 2.4	11.0 ± 2.3
Curvature (deg/μm)	5.3 ± 0.6	10.0 ± 2.3

Fig. 4

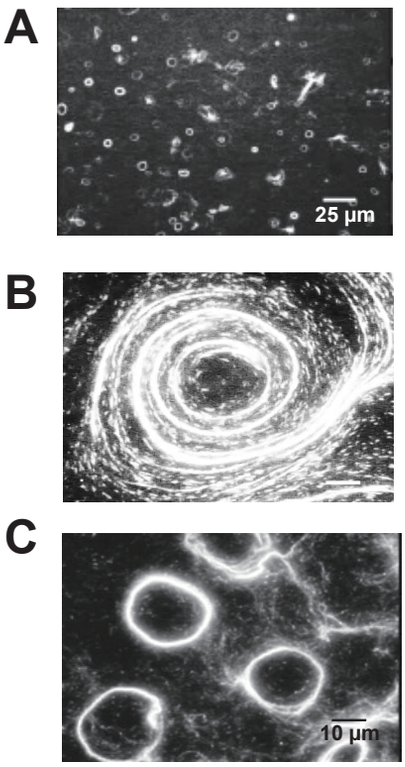

10 µm